Hindawi
Journal of Nanomaterials
Volume 2018, Article ID 5735609, 13 pages
https://doi.org/10.1155/2018/5735609

Research Article

Unexpected Stabilization of α-$Ni(OH)_2$ Nanoparticles in GO Nanocomposites

Josué M. Gonçalves,[1] **Kamilla M. Alves**,[2] **Manuel F. Gonzalez-Huila**,[1] **Alfredo Duarte**,[1] **Paulo R. Martins**,[2] **and Koiti Araki**[1]

[1]*Department of Fundamental Chemistry, Institute of Chemistry, University of Sao Paulo, Av. Lineu Prestes 748, 05508-000 Sao Paulo, SP, Brazil*
[2]*Instituto de Química, Universidade de Federal de Goiás, Goiânia, GO, Brazil*

Correspondence should be addressed to Josué M. Gonçalves; josuemartins@usp.br and Koiti Araki; koiaraki@iq.usp.br

Received 9 July 2018; Revised 10 August 2018; Accepted 28 August 2018; Published 18 December 2018

Academic Editor: Xuping Sun

Large specific charge capacity $Ni(OH)_2$@GO nanocomposites, able to withstand high current densities and more than 500 redox cycles without significant loss of charge storage capacity, were realized thanks to unexpected stabilization of electrochemically active α-$Ni(OH)_2$ nanoparticles by GO and were characterized by TEM, XRD, FTIR, TXRF, and confocal Raman microscopy. Stable and adherent films with low electric resistance, able to withstand current densities as high as 100 $A \cdot g^{-1}$, were generated, as demonstrated by CV, EIS, and galvanostatic charge-discharge measurements, showing good perspectives as electrode material for hybrid energy storage devices.

1. Introduction

Energy storage devices are fundamental components of the energy matrix nowadays because of the increasing number and variety of mobile and portable devices, especially the increasing demand from the transportation industry, whose growth is dependent on the continuous development of high-power, high-energy density, fast-charging-discharging, and excellent life cycle devices [1]. Supercapacitors and hybrid supercapacitors are promising high-performance devices to fulfil those demanding requirements.

There are two types of supercapacitors, double-layer electrochemical capacitors (EDLCs) and pseudocapacitors, where the former stores energy only by capacitive processes whereas the latter does it by Faradaic processes [2] but with a capacitor-like behaviour, i.e., a relatively constant capacitance is achieved within a potential window. Light- and high-surface area carbon-based materials tend to present large storage capacity at the electrode/electrolyte interface, as expected for high-power density and fast-charge-transfer materials, in addition to high chemical and mechanical stability. Unfortunately, though, despite all those very interesting properties, the energy density is not high enough for most applications. Accordingly, Faradaic processes must be also exploited in order to overcome such a drawback. In fact, transition metal oxides such as RuO_2 [3] and MnO_2 [4] are pseudocapacitive materials [5] with high specific redox capacitance but their charging-discharging speed is limited by the electronic/ionic conductivity. In addition, they tend to be less durable providing devices with shorter life cycles [6]; rare element- (such as ruthenium) based materials are expensive, and their production and supply are susceptible to some factors that are not under control. In this context, hybrid supercapacitors are interesting alternatives.

On the other hand, hybrid supercapacitors are energy storage devices achieved by putting together a supercapacitor and a battery-type electrode. This type of electrode is commonly coupled with electrical double-layer electrodes to combine the favorable characteristics of batteries (high energy density) with those of supercapacitors (high power output) [7]. The energy storage in battery-type electrode materials such as Co_3O_4, NiO, $ZnCo_2O_4$, Fe_2O_3, $NiCo_2O_4$,

and $Ni(OH)_2$ also is based on Faradaic processes, but their specific capacitance is strongly dependent on the voltage window, in contrast with that of supercapacitor materials, and thus, specific capacity [7–9] (in C/g or mA·h/g unit) should be adopted as the energy storage metric.

Lithium-based batteries and storage devices are already outperforming all others and are the ones with the fastest development curve, being the dominant technology nowadays. In fact, they present the highest charge density and are becoming more and more reliable and efficient. However, the lithium sources are limited [10] and located in few countries such as Chile, Argentina, and Bolivia (South America's "lithium triangle") [11], some suffering with frequent geopolitical issues that may undermine long-term initiatives. Accordingly, it is important to continue the development of reliable technological alternatives as strategic backup in eventualities since there is a prognostic that most of the annual production of lithium will be necessary for fabrication of only about half a million electric cars a year.

In this context, nickel hydroxide ($Ni(OH)_2$) has been extensively investigated as potential electrode material of hybrid supercapacitors [8, 9, 12, 13] and batteries [14], due to its high charge capacity, reliability, abundance, low toxicity, and safety as compared to flammable lithium-based materials. Nickel hydroxide can be found in the more disorganized alpha (α-$Ni(OH)_2$) and the more crystalline beta-phase (β-$Ni(OH)_2$). Beta nickel hydroxide is the thermodynamically most stable material which is converted to β-NiOOH in the charging process [15] of batteries. However, the β(II)/β(III) potential initially found at 530 mV is continuously shifted to more positive potentials as a function of time and the number of charge/discharge cycles, finally leading to the evolution of molecular oxygen (O_2) and consequent loss of efficiency [15].

The best choice would be turbostratic alpha-$Ni(OH)_2$ materials, when stabilized enough against the conversion to the thermodynamically most stable beta-phase material during storage and operation conditions, presenting a much larger conductivity and a theoretical specific capacity as high as 433 $mA{\cdot}h{\cdot}g^{-1}$. In fact, strategies based on the incorporation of different metal cations (Al [16], Mn [17], Fe [18, 19], Co [20], Cu [21], Zn [22], Y [23], Pb [24], Ce [25]); intercalation of anions (nitrate) [26–28], chloride [27], sulphate [27], cyanate [29], carbonate [29, 30], acetate [30], succinate [30], glutarate [30], and adipate [30]); and preparation of nanocomposites (with clays [31, 32], graphite [33], carbon nanotubes [5, 34], and reduced graphene oxide [35, 36]) were exploited in an attempt to improve the electrochemical properties and/or stability of nickel hydroxide in the alpha phase.

The reticular substitution of Ni^{2+} by other M^{2+} cations can induce localized defects, but when the substitution involves M^{3+} cations, the excess positive charge must be neutralized by OH^- or other intercalated anions or by release of protons. Nitrate is the most commonly intercalated anion among all other generating materials with the general formula $Ni(OH)_{2-x}A_yB_z{\cdot}nH_2O$, where A and B are, respectively, monovalent and divalent anions and $x = y + 2z$ [30, 37]. However, Lee et al. [28] demonstrated that bulky intercalated anions can inhibit ion diffusion and impair the electrochemical properties.

In a pioneering work in this field, M. S. Kim and K. B. Kim [38] confirmed the low stability of nickel hydroxide in the alpha phase, where a significant decrease of the peak current was observed right in the second voltammetric cycle, as consequence of its conversion to the beta phase. A more recent and interesting approach for stabilization of α-$Ni(OH)_2$ is the preparation of nanoparticle-based composites. Rocha et al. reported that α-$Ni(OH)_2$ can be stabilized by interaction with montmorillonite clay and heat treatment but the conversion to the beta phase was observed before 200 consecutive redox cycles [39]. More recently, Nunes et al. [32] realized a composite material in which the clay particles were covered up with α-$Ni(OH)_2$ nanoparticles, exhibiting improved electrochemical properties but relatively low conductivity and charge capacity.

In this context, light- and high-conductivity and surface area carbon materials such as graphite, carbon nanotubes, and graphene are more promising for the development of electrode materials for charge storage devices [40]. In fact, several are the reports on materials based on $Ni(OH)_2$ incorporated in reduced graphene oxide (rGO) exhibiting enhanced specific capacitance [1, 2, 20, 41–46]. For example, Zhu et al. described a $Ni(OH)_2$/rGO composite material for a battery anode with specific capacity as high as 1110 and 1500 $mA{\cdot}h{\cdot}g^{-1}$ for the first charge and discharge cycles but the discharge capacity decreased by 33% after only 40 cycles [46]. The lack of stability of α-$Ni(OH)_2$ nanoparticles incorporated in rGO was confirmed by Gonçalves et al. [20], where a 50% decay in stored energy was observed after 500 charge-discharge cycles. Similar results have been observed for analogous graphene nanocomposites suggesting that carbon nanomaterials may not stabilize nickel hydroxide in the alpha phase. Fortunately, this was not the case and nanocomposites based on α-$Ni(OH)_2$ nanoparticles and graphene oxide (GO) exhibiting quite distinct electrochemical behaviour, as well as enhanced specific capacity, are described now on.

2. Materials and Methods

2.1. Chemicals and Materials. All reagents and solvents were of analytical grade and used as received. Anhydrous glycerine, isopropyl alcohol, sulfuric acid, sodium nitrate, sodium borohydride, potassium permanganate, and potassium hydroxide were purchased from Synth Brazil. Nickel acetate tetrahydrate was purchased from Sigma-Aldrich, and *n*-butyl alcohol was acquired from Vetec. Graphite was purchased from Vonder.

Alpha-$Ni(OH)_2$ sol was prepared according to the method described by Rocha et al. [15, 39, 47] by reacting nickel acetate with KOH, in a 1 : 2 molar ratio. Typically, 9.68 g (0.389 M) of $Ni(CH_3COO)_2{\cdot}4H_2O$ was dissolved in 100 mL of glycerine at 50°C, under vigorous stirring, and cooled down to room temperature. Then 100 mL of KOH solution in BuOH (0.973 M) was added, and the mixture was stirred for 6 h for preparation of nickel hydroxide nanoparticles [39, 47, 48].

Graphite oxide (GrO) was prepared by modified Hummers' method [49, 50] summarized below. Concentrated H_2SO_4 (115 mL) was added to a mixture of graphite flakes (5.0 g) and $NaNO_3$ (2.5 g). Then $KMnO_4$ (15.0 g) was slowly added while the reaction mixture was kept at 50°C under stirring for 6 h. The reaction mixture was carefully diluted with 400 mL of water and then cooled in a water bath before further reaction with 20 mL of H_2O_2 solution (30% *v*/*v*). After 30 minutes, the reaction mixture was centrifuged (5000 rpm, 10 min) and the supernatant decanted away. The solid material was then successively washed and centrifuged (5000 rpm for 10 min) with 800 mL of 30% HCl solution and then with 400 mL of ethanol. The black solid was resuspended in 400 mL of diethyl ether, filtered out with a 0.45 μm PTFE membrane, and dried overnight at room temperature, in a desiccator under vacuum.

A GO dispersion was prepared by exfoliation of 500 mg of graphite oxide in 500 ml of deionized water in an ultrasonic bath for two hours, while adjusting the pH to 8.0 by addition of a saturated KOH solution. Then it was concentrated ten times using a flash evaporator in order to get a GO dispersion of 10 g·L^{-1}.

The α-Ni(OH)$_2$@GO nanocomposites were prepared based on a method that favors the interaction of the nickel hydroxide nanoparticles with GO sheets as follows. The α-Ni(OH)$_2$ sol in glycerol was slowly added into a GO suspension according to the proportions listed in Table 1, and the reaction mixture was stirred for 24 h at room temperature and atmospheric pressure.

The CV and EIS data were recorded using modified FTO glass electrodes, with area $A = 1$ cm^2, defined with Scotch tape and modified by spin coating at 2500 rpm immediately after transferring 25 μL of a nanomaterial suspension onto the surface and vacuum drying for 96 hours at room temperature, in order to produce adherent films in a reproducible way.

Galvanostatic charge-discharge (GCD) curves were registered using larger modified FTO glass electrodes ($A = 4$ cm^2) as prepared above by spin coating after transferring a suitable volume of nanocomposite suspension (containing 3–6 mg) onto the surface and vacuum drying for 96 hours at room temperature.

2.2. Apparatus and Characterizations. The samples were characterized by X-ray diffractometry (XRD) in a Bruker D2 or D8 PHASER diffractometer equipped with Cu Kα source ($\lambda = 1.5418$ Å, 30 kV, 15 mA, step = 0.05°), in the 2θ range from 5 to 70°. Infrared spectra were recorded in a Bruker ALPHA FTIR spectrophotometer. The concentration of Ni in the nanocomposite materials was determined by total reflection X-ray fluorescence spectroscopy (TXRF) (Bruker PICOFOX S2).

Transmission electron microscopy (TEM) images were obtained in a JEOL JEM-2100 equipment at an accelerating voltage of 200 kV. Samples were prepared on copper grids (Ted Pella) by dispersing 3 μL of suspension diluted with water.

Confocal Raman microscopy images were obtained using a WITec alpha 300R microscope equipped with Ar ion laser ($\lambda = 488$ nm, WITec), 100x objective (NA 0.80), 600 lines.mm^{-1} grating, and integration time of 0.2 s. Raman images were obtained mapping 50×50 μm areas (2500 points) using a piezo-driven xyz table, setting the laser power to 1.8 mW·cm^{-2} and the integration time to 0.2 s per point. The images were generated rendering based on the area under the 3665 cm^{-1} and 1350 cm^{-1} peaks assigned to Ni(OH)$_2$ and GO domains. The samples prepared on platinum wafer were also used to get the Raman chemical mapping images.

Table 1: Proportion of GO and α-Ni(OH)$_2$ nanoparticle dispersion in glycerol used in the preparation of α-Ni(OH)$_2$@GO nanocomposites.

Nanocomposite	GO (mL)	α-Ni(OH)$_2$ (mL)	Glycerol (mL)	Ni/GO ratio (m/m)
α-Ni(OH)$_2$	—	5.0	5.0	—
α1-Ni(OH)$_2$@GO	1.0	5.0	4.0	5.70
α2-Ni(OH)$_2$@GO	2.0	5.0	3.0	2.85

Cyclic voltammetry and electrochemical impedance spectroscopy (EIS) measurements were carried out using an Eco Chemie Autolab PGSTAT30 potentiostat/galvanostat and a conventional three-electrode cell, constituted by Ag/AgCl (3.0 mol·L^{-1} in KCl) reference, a platinum wire counter, and modified FTO working electrodes. Electrochemical impedance spectra were registered modulating the frequency of the sinusoidal potential wave from 0.01 to 50000 Hz, using an AC amplitude of 10 mV superimposed to a DC potential.

3. Results and Discussion

3.1. Physicochemical Characterization. Well-dispersed graphene oxide (GO) constituted by about 0.9 nm thick and up to micrometer-large sheets (Figures 1(c)–1(e)) was successfully prepared by exfoliation of graphite oxide, as confirmed by transmission electron microscopy (TEM) and atomic force microscopy (AFM). Mirror-like polished glassy carbon (GC) electrodes were easily modified with this material forming compact films with wrinkles (Figures 1(a) and 1(b)) as expected for a flexible layered material, as shown by scanning electron microscopy (SEM).

The successful oxidation of graphite to graphite oxide was also confirmed by the conversion of the sharp XRD peak at 26.6° ($d = 3.4$ Å, Figure S1) in the first one to a broad 001 peak at 13.0° (Figure 2), corresponding to a basal plane spacing (d) equal to 6.8 Å, as expected for the presence of structural defects in Gr-O [51]. The low-intensity peaks at $2\theta = 12.5°$ and 24.9° can be assigned to impurities in the graphite from Vonder.

Nickel hydroxide nanoparticles exhibited broad peaks assigned to the 003, 006, 101, and 110 reflection characteristic of α-Ni(OH)$_2$ at $2\theta = 9.06°$ ($d = 9.79$ Å), 18.38°, 23°, and 60°. The 003 peak was broadened and shifted in α1-Ni(OH)$_2$@GO and α2-Ni(OH)$_2$@GO to 10.66° (8.33 Å) and 10.46° (8.49 Å), respectively (Table 2), indicating quite a

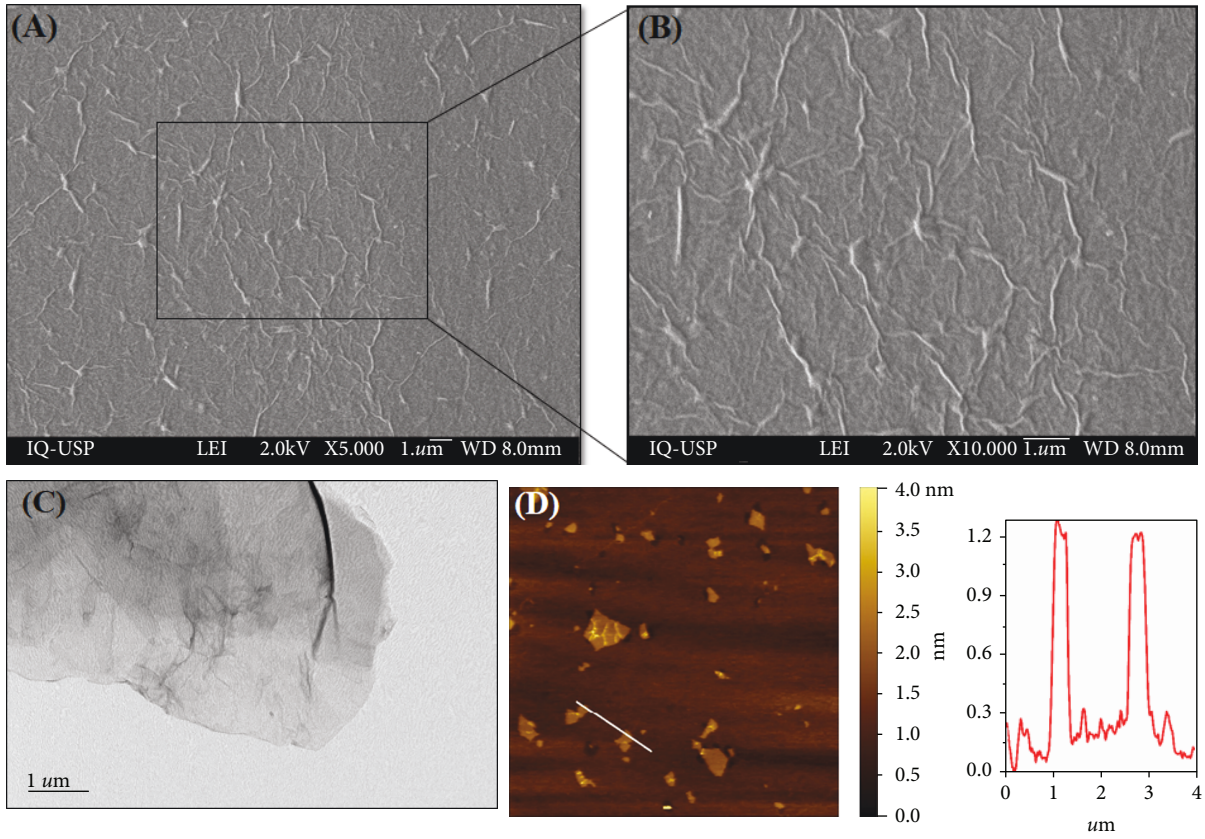

Figure 1: Microscopy images of a GO sample obtained by SEM (a) 5.000x and (b) 10.000x, (c) TEM and (d) AFM, and (e) AFM cross-section height profile at the line indicated in (d).

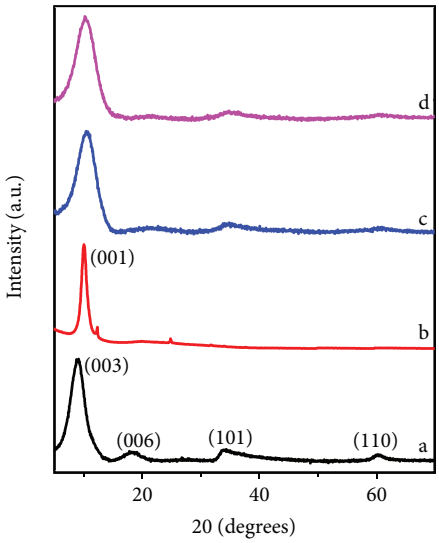

Figure 2: X-ray diffractograms of (a) α-$Ni(OH)_2$, (b) Gr-O, (c) α1-$Ni(OH)_2$@GO, and (d) α2-$Ni(OH)_2$@GO. The low-intensity peaks at $2\theta = 12.5^\circ$ and 24.9° are due to impurities in the graphite from Vonder.

strong interaction of the GO sheets with the α-$Ni(OH)_2$ nanoparticles, leading to a decrease in the basal plane distance and probably increase in the degree of disorder in the turbostratic nickel hydroxide structure. The peaks (003, 006, 101, and 110) were indexed according to the JCPDS #38-0715 catalogue card.

The nanomaterials were also characterized by confocal Raman spectroscopy. As expected, the spectra exhibited strong peaks typical of the D, G, D′, G′, and D+G bands (Figure 3(a)), confirming the success of the graphite oxidation reaction producing graphite oxide (Gr-O, the precursor of GO, Figure S2A). The D band, generated by double Raman resonance processes, was found at 1350 cm^{-1} and is characteristic of sp^2 carbon aromatic ring respiration modes in structurally disordered regions, in addition to edge effects (Figure 3(a), ii) [35]. On the other hand, the G band at 1600 cm^{-1} is generally assigned to the first-order scattering of phonons associated within plane E_{2g} stretching modes of sp^2 carbon atoms [35, 52]. The position and relative intensity of those bands are directly related to the degree of graphitization, whereas their broadening indicates a larger structural disorder. In Figure 3(a), ii, and also in Figure S2A (supporting info), the presence of the G′, D′, and D+G bands of GO is evident at 2720, 2940, and 3190 cm^{-1}, respectively, where the G′ band is related to the two-dimensional organization in the graphene plane. The I_D/I_G ratio of 1.0 found for our graphene oxide indicates a high concentration of "structural defects," as consequence of the graphite oxidation

Table 2: The 2θ values and respective basal plane distances corresponding to the (003), (006), (101), and (110) reflection planes of α-$Ni(OH)_2$, α1-$Ni(OH)_2$@GO, and α2-$Ni(OH)_2$@GO.

Nanocomposite	2θ (003)–d (Å)	2θ (006)–d (Å)	2θ (101)–d (Å)	2θ (110)–d (Å)
α-$Ni(OH)_2$	9.06°–9.79 Å	18.38°–4.89 Å	34.32°–2.73 Å	60.39°–1.77 Å
α1-$Ni(OH)_2$@GO	10.66°–8.33 Å	21.69°–4.17 Å	34.97°–2.69 Å	60.84°–1.76 Å
α2-$Ni(OH)_2$@GO	10.46°–8.49 Å	21.59°–4.19 Å	35.32°–2.68 Å	61.05°–1.76 Å

by Hummers method converting sp^2 (planar) to sp^3 (tetrahedral) carbons.

In contrast with GO, α-$Ni(OH)_2$ exhibits a relatively low Raman scattering cross-section probably as consequence of the large structural disorder [20] (Figure S2B) and strong interaction with water, acetate anion, and glycerol molecules, making it very difficult to detect the nickel hydroxide in the nanocomposites by this technique (Figure 3(a), iii and iv). The best result was achieved by confocal Raman microscopy imaging of α1-$Ni(OH)_2$@GO that allowed the identification of nickel hydroxide-rich pixels, shown in green (Figure 3(b)), by image rendering based on the area under the 3665 cm^{-1} peak, assigned to the stretching mode of OH^- bound to Ni(II) ion. In fact, the image provides a chemical mapping of the scanned area where each pixel is a complete Raman spectrum. Since no similar features were observed for α2-$Ni(OH)_2$@GO, that result is a strong indication that α-$Ni(OH)_2$ nanoparticles may be forming small clusters on the GO sheets at higher concentrations.

Infrared spectroscopy showed to be a better technique in monitoring the presence of nickel hydroxide in the nanocomposites. Alpha-$Ni(OH)_2$ (Figure 3(c), i) showed an intense and broad band at 3435 cm^{-1} characteristic of the axial stretching of the −OH group and a sharp band assigned to the symmetric stretching mode of methyl groups in 2853 cm^{-1}, as expected for the presence of glycerine [25, 35]. The intense band at 638 cm^{-1} was associated to the in-plane angular deformation of the O-Ni-O bond. On the other hand, GO (Figure 3(c), ii) showed an intense and broad band at 3445 cm^{-1} attributed to the axial deformation of the −OH group confirming the relatively high degree of oxidation of the GO sheets. In addition, the band at 1635 cm^{-1} is typical of aromatic C=C bonds, whereas the one at 1340 cm^{-1} can be assigned to C-OH stretching modes [53]. The FTIR spectrum of the composites was similar, but the larger proportion of GO increased the relative intensity of the 3445 and 1635 cm^{-1} bands characteristic of the −OH and C=C stretching modes, respectively. The presence of the 1411, 1117, and 1060 cm^{-1} bands attributed to C-C and C-C-H and C-C-O angular deformation modes was clearly observed also. The presence of α-$Ni(OH)_2$ nanoparticles decorating GO sheets is additionally confirmed by the 638 cm^{-1} band associated with the in-plane angular deformation of Ni-O bonds (Figure 3(c), iii and iv).

The nanocomposites were also characterized in detail by transmission electron microscopy, and the images correspondent to α2-$Ni(OH)_2$@GO (Ni/GO = 2.85 m/m) clearly show a material where the GO sheets are dense and homogeneously decorated with a layer of nickel hydroxide nanoparticles (Figure 4(c)), but with some small aggregates in the case of α1-$Ni(OH)_2$@GO (Figures 4(a) and 4(b), Ni/GO = 5.70 m/m), as expected for the larger nanoparticle/GO ratio in it, in agreement with the respective confocal Raman microscopy images. These results associated with the fact that no significant amount of nickel hydroxide is released into water or KOH solution confirming the strong interaction of α-$Ni(OH)_2$ nanoparticles with the GO surface, a very important feature considering electrochemical applications.

Interplanar spacing equal to 2.05 Å was determined by analysis of the interference fringes on individual nanoparticles imaged by HRTEM (Figures 4(d) and 4(e)). This value contrasts with that expected for nickel hydroxide (α-$Ni(OH)_2$ $d = 7.5$ Å and β-$Ni(OH)_2$ $d = 4.6$ Å) but is in agreement with face-centered cubic NiO [54], as confirmed by the presence of the characteristic 111, 200, 220, and 311 planes in the selected area diffraction pattern (SADP). This material is produced by in situ dehydroxylation/dehydration processes [24, 35] of $Ni(OH)_2$ as consequence of the local heating caused by the electron beam focused on the sample during the TEM imaging and low pressure inside the microscope analysis chamber.

On the other hand, the attempts to get the EDS mapping of the nanocomposites were hindered by the continuous movement of the quite fragile GO sheets decorated with $Ni(OH)_2$ nanoparticles under the influence of the electron beam. Nevertheless, α1-$Ni(OH)_2$@GO was successfully characterized by EDS confirming the presence of nickel, oxygen, and carbon (Figure S3B, blue line) in area 2 (Figure S3A) confirming the presence of Ni hydroxide nanoparticles and GO, whereas none of those signals (Figure S3B, red line) could be found in a region with no nanocomposite (Figure S3A, area 1) as expected.

3.2. Electrochemical Properties. The electrochemical behaviour of electrodes modified with α-$Ni(OH)_2$ nanoparticles and α1 and α2-$Ni(OH)_2$@GO nanocomposites was evaluated by cyclic voltammetry (CV), electrochemical impedance spectroscopy (EIS), and galvanostatic charge-discharge (GCD) techniques. The electrodes were subjected to 500 cycles of potential scan, in the +0.1 to +0.55 V range, at 50 $mV{\cdot}s^{-1}$, in 1.0 $mol{\cdot}L^{-1}$ KOH solution. In all cases, there was a shift of the oxidation peak potential (E_{ap}) corresponding to the $Ni^{II}(OH)_2/Ni^{III}(OOH)$ process as a function of the number of scan cycles. This tendency is more evident for the pure α-$Ni(OH)_2$ that also exhibited a significant decrease of the anodic (i_{ap}) and cathodic (i_{cp}) peak currents after 500 voltammetric cycles (Figure 5(a)) that was assigned to the

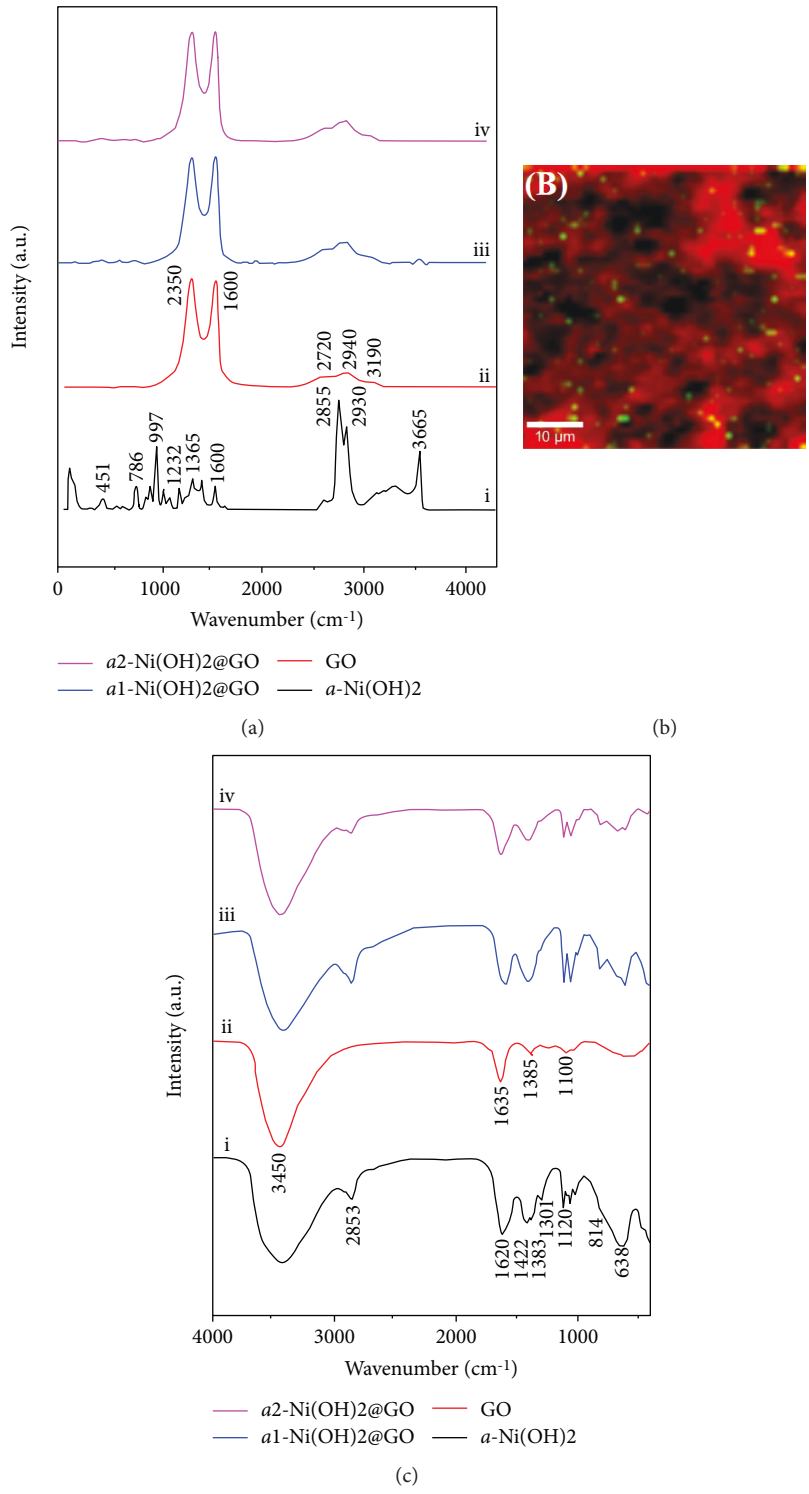

FIGURE 3: (a) Raman and (c) FTIR spectra of the (i) pure α-Ni(OH)$_2$ and (ii) pure GO, (iii) α1-Ni(OH)$_2$@GO and (iv) α2-Ni(OH)$_2$@GO, and (b) confocal Raman microscopy image of α1-Ni(OH)$_2$@GO.

slow conversion of nickel hydroxide from the alpha to the beta phase [20].

The α1- and α2-Ni(OH)$_2$@GO derivatives exhibited similar behaviour reaching the maximum peak current after about 100 cycles that was maintained until up to the 500th redox cycle, as shown in Figures 5(b)–5(d). Both presented larger charge capacity and stability than the pure nanoparticle. This behaviour suggests that the strong interaction of nickel hydroxide with GO is stabilizing it in the alpha phase, slowing down its transformation to the beta phase. It is also interesting to notice that the presence of larger relative amounts of GO impaired in some extent the electrochemical

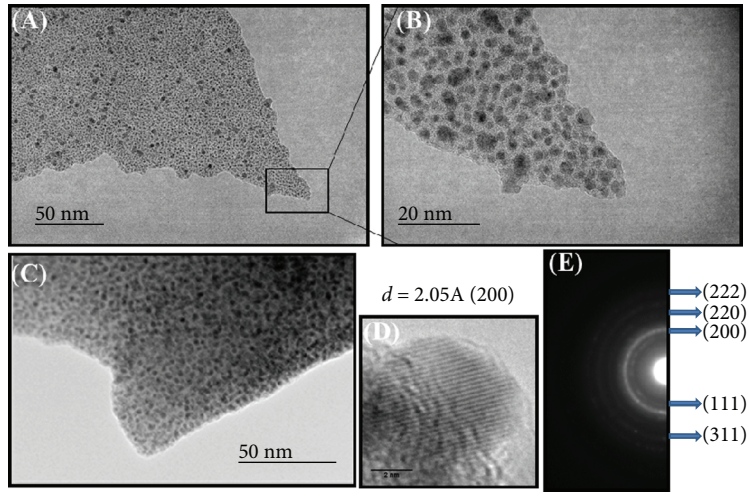

FIGURE 4: (a, b) TEM images of the α1-Ni(OH)$_2$@GO nanocomposite in two magnifications from left to right and (c) α2-Ni(OH)$_2$@GO, (d) corresponding HRTEM image, and (e) diffraction pattern of a selected area and corresponding diffraction planes.

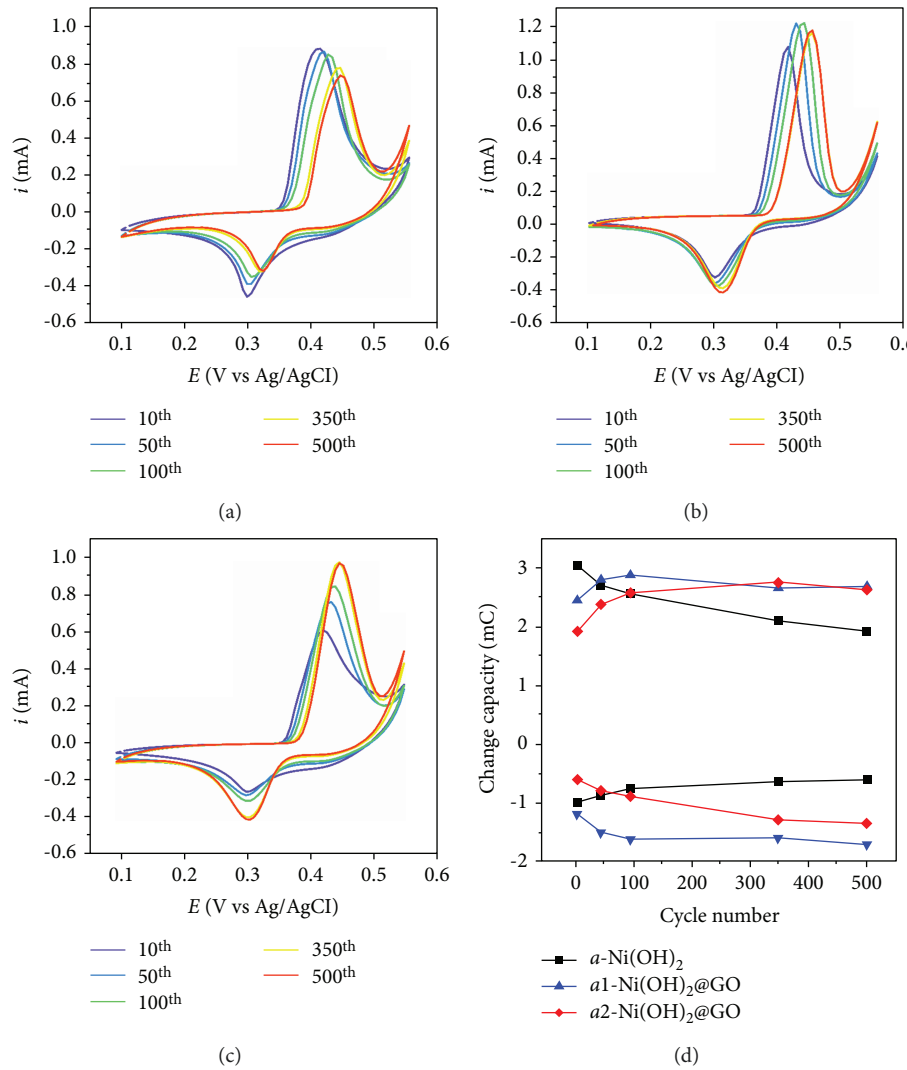

FIGURE 5: Evolution of the cyclic voltammograms of electrodes modified with (a) α-Ni(OH)$_2$, (b) α1-Ni(OH)$_2$@GO, and (c) α2-Ni(OH)$_2$@GO along 500 redox cycles at 50 mV·s^{-1}, in 1.0 mol·L^{-1} KOH solution and respective (d) plot of charge capacity vs the number of redox cycles.

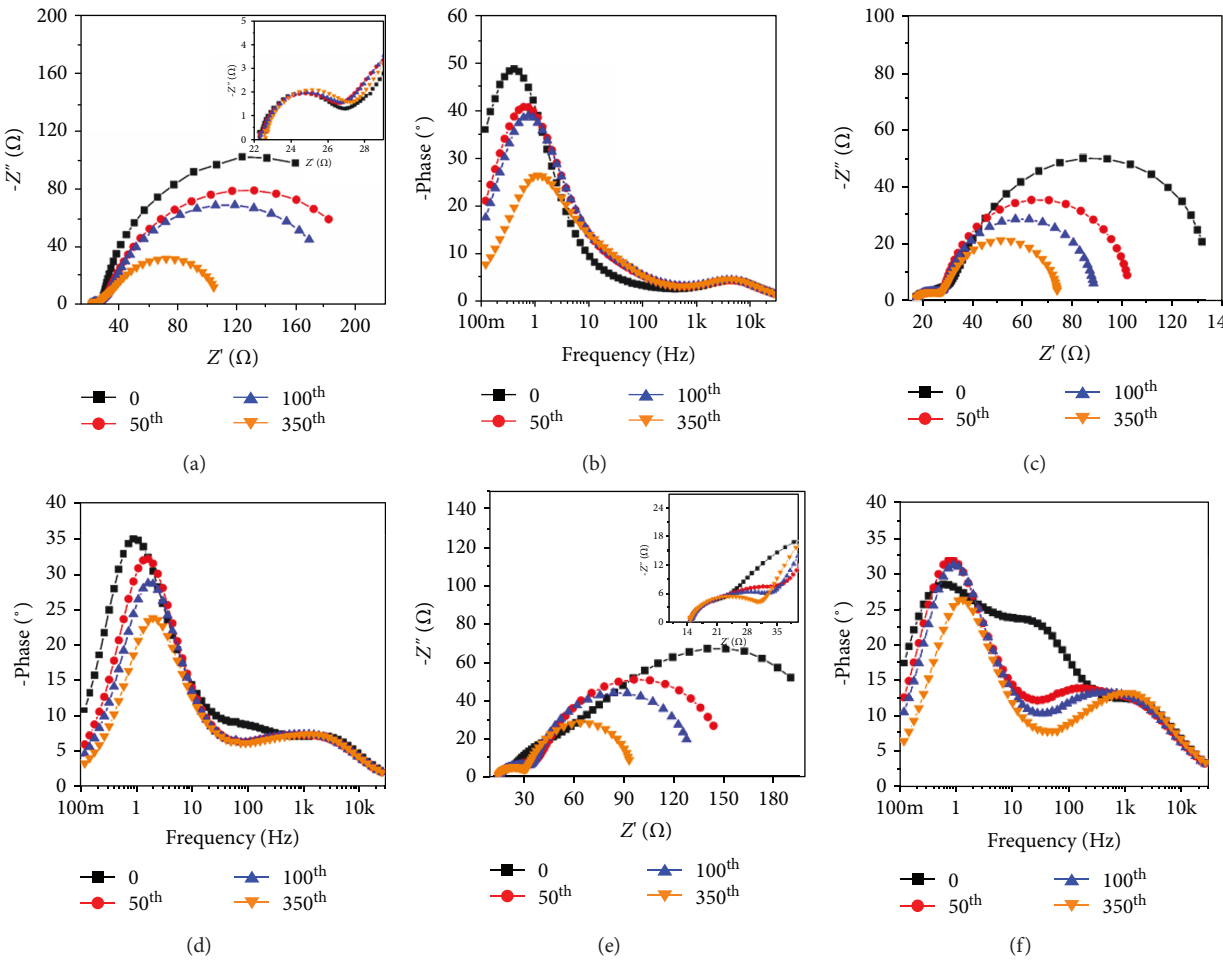

FIGURE 6: (a, c, e) Nyquist and (b, d, f) Bode phase diagrams of α-$Ni(OH)_2$ (a, b), α1-$Ni(OH)_2$@GO (c, d), and α2-$Ni(OH)_2$@GO (e, f) as a function of the number of redox cycles, up to 350 cycles. The EIS measurements were carried out after 0, 50, 100, and 350 cycles, at 0.55 V DC potential, and superimposed AC signal with $\Delta E = 10$ mV, in the 0.01 to 50000 Hz range.

properties, probably as consequence of the presence of low-permeability GO sheets acting as barriers for the diffusion of the electrolyte (K^+ and OH^- ions). This is reflecting on the fact that only 80% of the redox sites seem to be reached and activated in the α2-$Ni(OH)_2$@GO nanocomposite after 100 voltammetric cycles (Figure 5(c)). A more detailed perspective can be realized analysing Figure 5(d) where the plots of the amount of charge under the anodic and cathode voltammetric curves were plotted as a function of the number of voltammetric cycles, making clear the higher stability of the nanocomposites as well as the slower activation of the redox sites in the α2-$Ni(OH)_2$@GO derivative. The higher stability of this material (Ni/GO = 2.85 m/m) can be related to the more homogeneous distribution of the nanoparticles on the GO sheets and consequent larger interaction between the oxygen atom on the nanosheets and the $Ni(OH)_2$ nanoparticles.

The electrochemical properties of the modified electrodes can be better understood upon EIS analysis (Figure 6). The Nyquist diagrams and Bode phase spectra of α-$Ni(OH)_2$ after 0, 50, 100, and 350 successive redox cycles in the +0.0 to +0.55 V range exhibited two semicircles (Figure 6(a)). The first activated process at high frequencies was attributed to the $Ni^{II}(OH)_2/Ni^{III}(OOH)$ process, whereas the second one at lower frequencies was associated with the heterogeneous electron transfer process at the film/solution interface, more specifically to the oxidation of water catalysed by the nanomaterials, since the +0.55 V applied DC potential is near the onset potential of that reaction. It is interesting to observe that the impedance of the first one increased steadily whereas the impedance of the second process decreased significantly, especially after the 100th cycle up to the 500th cycle, as confirmed by the decrease of the corresponding semicircle diameter.

The nanocomposites exhibited a larger resistance associated with the Ni^{3+}/Ni^{2+} process and a continuous decrease of the resistance of the OER demonstrating that the catalytic activity of the nanomaterials is enhanced by aging. This is reflected on the shift of the associated peak in the Bode phase plot to higher frequencies. In addition, the Nyquist spectra simulation revealed a diffusion-controlled process in the α2-$Ni(OH)_2$@GO spectra, represented by a short linear segment with a slope of approximately 0.5 in the region in between the two semicircles, attributed to the diffusion of electrons through the nanocomposite film, as expected for a slower electrolyte diffusion in this material.

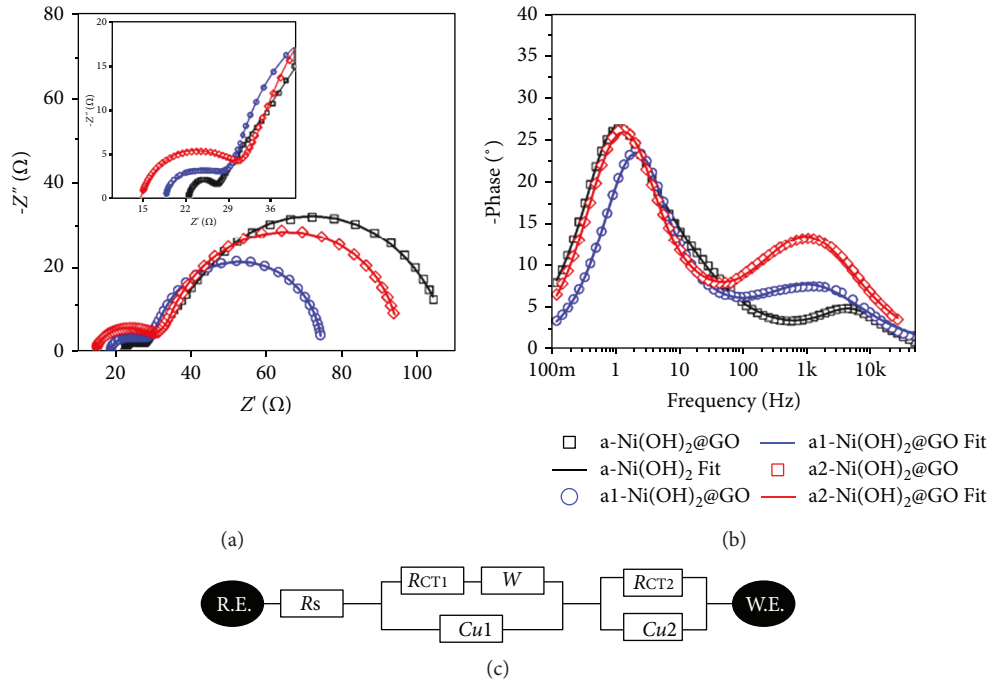

Figure 7: (a) Nyquist and (b) Bode phase plots of EIS data registered for α-Ni(OH)$_2$, α1-Ni(OH)$_2$@GO, and α2-Ni(OH)$_2$@GO after 350 CV cycles, intercalated by EIS measurements at a DC potential of 0.55 V, superimposing an AC perturbation of $\Delta E = 10$ mV, in the 0.01 to 50,000 Hz range. The equivalent circuit used to fit all EIS data is shown in (c).

Table 3: Resistance and capacitance parameters (R_S, R_{CT1}, R_w, $C_{\mu 1}$, R_{CT2}, and $C_{\mu 2}$) determined upon simulation of the EIS data using the equivalent circuit shown in Figure 7(c).

Electrode modifier	R_S (Ω)	R_{CT1} (Ω)	R_W (Ω)	$C_{\mu 1}$ (μF)	R_{CT2} (Ω)	$C_{\mu 2}$ (mF)
α-Ni(OH)$_2$	16.1	6.72	7.75	8.28	74.5	3.43
α1-Ni(OH)$_2$@GO	18.5	9.97	17.9	0.168	28.4	5.25
α2-Ni(OH)$_2$@GO	14.7	16.3	21.6	0.153	42.6	6.54

The higher stability of the α1-Ni(OH)$_2$@GO nanocomposite is confirmed by the invariance of the diameter of the small semicircle at high frequencies, in comparison with that of pure α-Ni(OH)$_2$ and α2-Ni(OH)$_2$@GO. The decrease of the resistance in the diffusion-controlled region as a function of the number of voltammetric cycles is apparent, as expected for the activation of the increasing number of redox sites in the film probably as consequence of the electrolyte diffusion.

All electrochemical properties can be more easily understood upon analyses of the EIS behaviour (Nyquist diagrams) registered for the nickel hydroxide nanomaterials after 350 voltammetric cycles (Figure 7). Clearly, the incorporation of low-conductivity GO is increasing the resistance of the Ni(OH)$_2$/NiOOH process (Table 3), as confirmed by the larger phase angle and lower frequency of the corresponding process in the Bode phase spectrum (Figure 7(b)). In contrast, GO decreased significantly the heterogeneous charge transfer resistance for oxidation of water, as confirmed by the tendency to diminish the diameter of the semicircle at lower frequencies (Figure 7(a)). Nevertheless, the activity is maximized in α1-Ni(OH)$_2$@GO, decreasing for α2-Ni(OH)$_2$@GO. The Nyquist and Bode phase diagrams were simulated using the equivalent circuit shown in Figure 7(c), to get the R_s, R_{CT1}, R_w, $C\mu 1$, R_{CT2}, and $C_{\mu 2}$ parameters listed in Table 3.

One of the possible applications of battery-type nickel-based nanomaterials is in hybrid supercapacitors (for example, paired with an activated carbon electrode), where the capacity must be high to fulfill the stringent requirements in several working conditions or, in other words, in a wide range of current densities (fast charge/discharge capacities) and long life cycle. The curves of specific capacity as a function of current density shown in Figure 8(d) indicate a tendency of steady decrease as a function of the current density, a profile commonly found in battery-type electrode materials. In addition, the discharge time was elongated after 500 voltammetric cycles, indicating an improvement of the specific capacity relative to the mass of nickel. In fact, the specific capacity of the α1-Ni(OH)$_2$@GO and α2-Ni(OH)$_2$@GO nanocomposites at 100 A·g^{-1}, a quite large current density, was found to be 639 and 553 C·g^{-1}, respectively, significantly larger than for pure Ni(OH)$_2$ nanoparticles (351 C·g^{-1}). This result is consistent with the enhanced stability of the nickel hydroxide nanoparticles in the alpha phase in the nanocomposites and clearly demonstrates the synergic contribution of the double-layer capacitance of GO to the charge capacity. In fact, Figures 8(a)–8(c) and Figure S3 show discharge curves with plateaus (battery-type behaviour) and a sloping region characteristic of capacitive behaviour [55]. The small areas

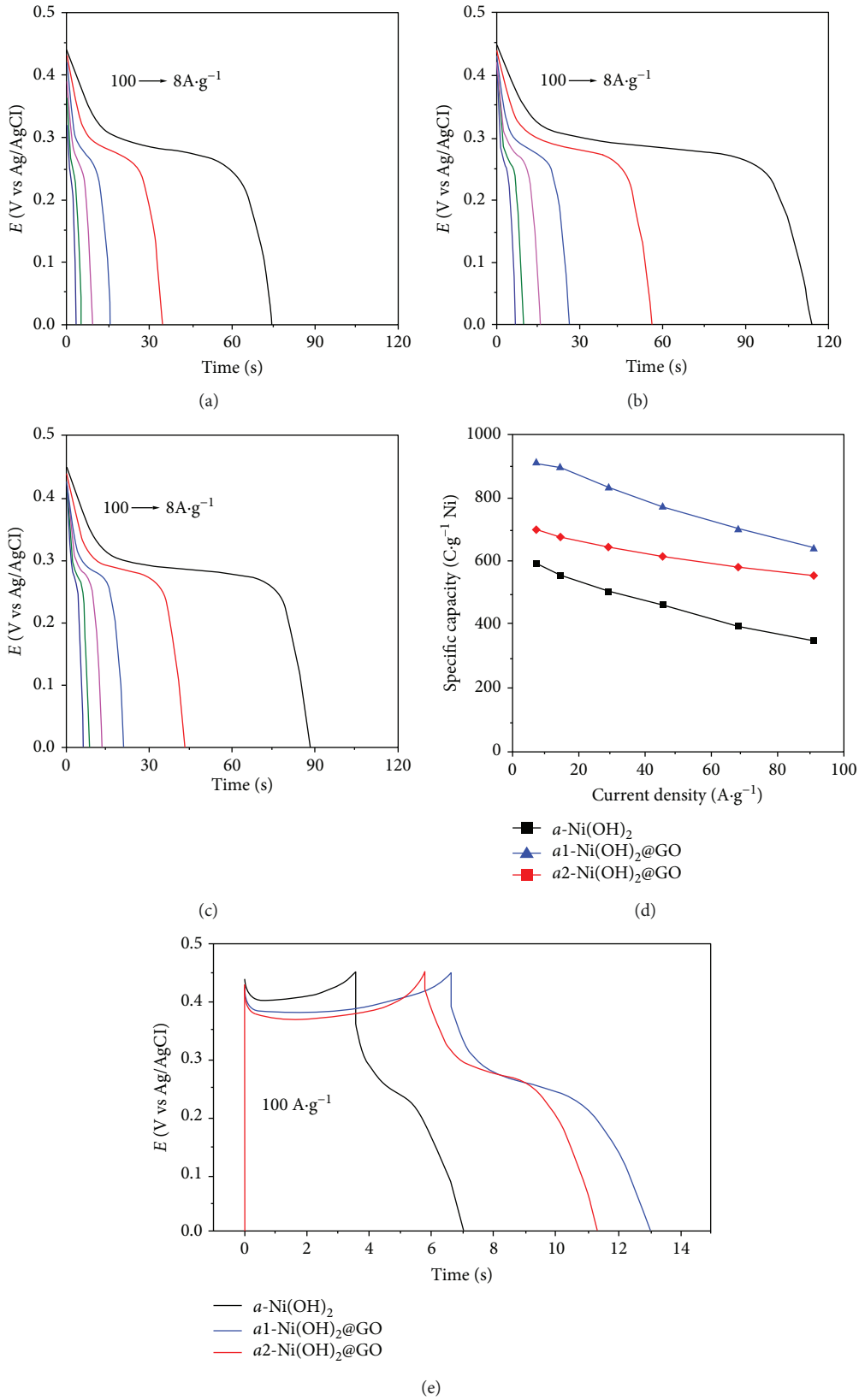

FIGURE 8: Discharge curves determined for (a) α-$Ni(OH)_2$, (b) α1-$Ni(OH)_2$@rGO, and (c) α2-$Ni(OH)_2$@rGO at increasing current densities (8, 16, 32, 50, 75, and 100 $A{\cdot}g^{-1}$), (d) respective plots of the specific capacity as a function of the current density, and (e) discharge curves determined for α-$Ni(OH)_2$, α1-$Ni(OH)_2$@rGO, and α2-$Ni(OH)_2$@rGO at 100 $A{\cdot}g^{-1}$.

associated with it (Figure S4) indicate a small contribution of the electric double-layer capacitance of GO, as expected for a material with lower electrical conductivity, as confirmed by previous reports [56, 57]. The large surface area of the 5-6 nm-diameter α-$Ni(OH)_2$ nanoparticles favors fast redox processes, as well as electron and electrolyte diffusion in the nanostructured materials [20]. In addition, the material can be charged and discharged at high current densities like a capacitor, being able to withstand discharge rates as high as 100 $A{\cdot}g^{-1}$ for long enough time to be considered for most applications (Figure 8(e)).

4. Conclusion

The α-$Ni(OH)_2$@GO nanocomposites exhibited high specific charge capacity and current density, as well as good stability even after 500 redox cycles, in contrast with α-$Ni(OH)_2$ composites with reduced graphene oxide or graphite in which the process of conversion to the beta phase seems to be accelerated. That unexpected result was assigned to the much stronger interaction of α-$Ni(OH)_2$ nanoparticles with GO surface generating nanocomposites in which each sheet is covered up with the electrochemically active nanomaterial, as revealed by TEM, XRD, FTIR, TXRF, and confocal Raman microscopy. The packing of such α-$Ni(OH)_2$@GO particles generates homogeneous and stable nanostructured films with low electric resistance able to withstand current densities as high as 100 $A{\cdot}g^{-1}$, as demonstrated by CV, EIS, and galvanostatic charge-discharge measurements.

Data Availability

The findings of this study are available from the corresponding author upon request, and some are included within the supplementary information file(s).

Conflicts of Interest

The authors declare that they have no conflicts of interest.

Acknowledgments

The authors are grateful to the Brazilian agencies "Conselho Nacional de Desenvolvimento Científico e Tecnológico" (CNPq) and "Fundação de Amparo à Pesquisa do Estado de São Paulo (FAPESP) for the financial support (CNPq 401581/2016-0, FAPESP 2013/24725-4) and fellowship (JMG CNPq 141853/2015-8). We also acknowledge PETROBRAS for the confocal Raman microscope. We also thank Dr. Marcelo Nakamura for the AFM images.

Supplementary Materials

Figure S1 shows the X-ray diffractogram of graphite. Figure S2 shows the Raman spectra of the (A) graphite and graphite oxide (Gr-O) and (B) α-Ni(OH)2 nanoparticles. Figure S3 shows the TEM image of sheet α1-Ni(OH)2@GO (A) and the EDS spectrum (B) of area without (1) and with (2) the composite. Figure S4 depicts the discharge curve determined for α1-Ni(OH)2@rGO at 8 A·g-1 showing the plateau region (battery-type behaviour) and the sloping regions characteristic of capacitive behaviour. *(Supplementary Materials.)*

References

[1] Y. Liu, R. Wang, and X. Yan, "Synergistic effect between ultra-small nickel hydroxide nanoparticles and reduced graphene oxide sheets for the application in high-performance asymmetric supercapacitor," *Scientific Reports*, vol. 5, no. 1, article 11095, 2015.

[2] J. L. Zhang, H. D. Liu, L. H. Huang, S. Z. Tan, W. J. Mai, and X. Cai, "Pre-stabilized reduced graphene oxide by ammonia as carrier for $Ni(OH)_2$ with excellent electrochemical property," *Journal of Solid State Electrochemistry*, vol. 19, no. 1, pp. 229–239, 2015.

[3] V. K. A. Muniraj, C. K. Kamaja, and M. V. Shelke, "$RuO_2{\cdot}nH_2O$ nanoparticles anchored on carbon nano-onions: an efficient electrode for solid state flexible electrochemical supercapacitor," *ACS Sustainable Chemistry & Engineering*, vol. 4, no. 5, pp. 2528–2534, 2016.

[4] X. Zhao, L. Zhang, S. Murali et al., "Incorporation of manganese dioxide within ultraporous activated graphene for high-performance electrochemical capacitors," *ACS Nano*, vol. 6, no. 6, pp. 5404–5412, 2012.

[5] M. Li, K. Y. Ma, J. P. Cheng, D. Lv, and X. B. Zhang, "Nickel–cobalt hydroxide nanoflakes conformal coating on carbon nanotubes as a supercapacitive material with high-rate capability," *Journal of Power Sources*, vol. 286, pp. 438–444, 2015.

[6] D. Feng, T. Lei, M. R. Lukatskaya et al., "Robust and conductive two-dimensional metal–organic frameworks with exceptionally high volumetric and areal capacitance," *Nature Energy*, vol. 3, no. 1, pp. 30–36, 2018.

[7] W. Jiang, F. Hu, Q. Yan, and X. Wu, "Investigation on electrochemical behaviors of $NiCo_2O_4$ battery-type supercapacitor electrodes: the role of an aqueous electrolyte," *Inorganic Chemistry Frontiers*, vol. 4, no. 10, pp. 1642–1648, 2017.

[8] A. Balducci, D. Belanger, T. Brousse, J. W. Long, and W. Sugimoto, "Perspective—a guideline for reporting performance metrics with electrochemical capacitors: from electrode materials to full devices," *Journal of the Electrochemical Society*, vol. 164, no. 7, pp. A1487–A1488, 2017.

[9] T. Brousse, D. Bélanger, and J. W. Long, "To be or not to be pseudocapacitive?," *Journal of the Electrochemical Society*, vol. 162, no. 5, pp. A5185–A5189, 2015.

[10] T. Prior, P. A. Wäger, A. Stamp, R. Widmer, and D. Giurco, "Sustainable governance of scarce metals: the case of lithium," *Science of The Total Environment*, vol. 461-462, pp. 785–791, 2013.

[11] R. O'Brien and R. Nickel, "Battery-hungry world turns to South America's 'lithium triangle'," 2016, https://www.reuters.com/article/us-latam-lithium/battery-hungry-world-turns-to-south-americas-lithium-triangle-idUSKCN0WH1BZ.

[12] B. Hu, X. Qin, A. M. Asiri, K. A. Alamry, A. O. Al-Youbi, and X. Sun, "Fabrication of $Ni(OH)_2$ nanoflakes array on Ni foam as a binder-free electrode material for high performance supercapacitors," *Electrochimica Acta*, vol. 107, pp. 339–342, 2013.

[13] Z. Pu, Q. Liu, A. H. Qusti, A. M. Asiri, A. O. Al-Youbi, and X. Sun, "Fabrication of $Ni(OH)_2$ coated ZnO array for high-rate pseudocapacitive energy storage," *Electrochimica Acta*, vol. 109, pp. 252–255, 2013.

[14] J. Tian, Z. Xing, Q. Chu et al., "PH-driven dissolution–precipitation: a novel route toward ultrathin $Ni(OH)_2$ nanosheets array on nickel foam as binder-free anode for Li-ion batteries with ultrahigh capacity," *CrystEngComm*, vol. 15, no. 41, pp. 8300–8305, 2013.

[15] M. Danczuk, C. V. Nunes Jr., K. Araki, and F. J. Anaissi, "Influence of alkaline cation on the electrochemical behavior of stabilized alpha-$Ni(OH)_2$," *Journal of Solid State Electrochemistry*, vol. 18, no. 8, pp. 2279–2287, 2014.

[16] H.-Y. Wu, Y.-L. Xie, and Z.-A. Hu, "Synthesis, characterization and electrochemical properties of board-like Al-substituted alpha nickel hydroxides," *International Journal of Electrochemical Science*, vol. 8, pp. 1839–1848, 2013.

[17] J. Lin, H. Jia, H. Liang et al., "Hierarchical $CuCo_2S_4$@NiMn-layered double hydroxide core-shell hybrid arrays as electrodes for supercapacitors," *Chemical Engineering Journal*, vol. 336, pp. 562–569, 2018.

[18] M. Gong, Y. Li, H. Wang et al., "An advanced Ni–Fe layered double hydroxide electrocatalyst for water oxidation," *Chemical Society*, vol. 135, no. 23, pp. 8452–8455, 2013.

[19] D.-c. Xia, L. Zhou, S. Qiao et al., "Graphene/Ni–Fe layered double-hydroxide composite as highly active electrocatalyst for water oxidation," *Materials Research Bulletin*, vol. 74, pp. 441–446, 2016.

[20] J. M. Gonçalves, R. R. Guimarães, C. V. Nunes Jr. et al., "Electrode materials based on α-$NiCo(OH)_2$ and rGO for high performance energy storage devices," *RSC Advances*, vol. 6, no. 104, pp. 102504–102512, 2016.

[21] J. Bao, Y. J. Zhu, Q. S. Xu et al., "Structure and electrochemical performance of Cu and Al codoped nanometer α-nickel hydroxide," *Advanced Materials Research*, vol. 479–481, pp. 230–233, 2012.

[22] Z. You, K. Shen, Z. Wu, X. Wang, and X. Kong, "Electrodeposition of Zn-doped α-nickel hydroxide with flower-like nanostructure for supercapacitors," *Applied Surface Science*, vol. 258, no. 20, pp. 8117–8123, 2012.

[23] J. Ren, Z. Zhou, X. P. Gao, and J. Yan, "Preparation of porous spherical α-$Ni(OH)_2$ and enhancement of high-temperature electrochemical performances through yttrium addition," *Electrochimica Acta*, vol. 52, no. 3, pp. 1120–1126, 2006.

[24] A. L. Correa, J. M. Gonçalves, P. O. Rossini et al., "Fast and reliable BIA/amperometric quantification of acetylcysteine using a nanostructured double hydroxide sensor," *Talanta*, vol. 186, pp. 354–361, 2018.

[25] J. M. Gonçalves, R. R. Guimarães, B. B. N. S. Brandão et al., "Nanostructured alpha-NiCe mixed hydroxide for highly sensitive amperometric prednisone sensors," *Electrochimica Acta*, vol. 247, pp. 30–40, 2017.

[26] C. C. Streinz, A. P. Hartman, S. Motupally, and J. W. Weidner, "The effect of current and nickel nitrate concentration on the deposition of nickel hydroxide films," *Journal of the Electrochemical Society*, vol. 142, no. 4, pp. 1084–1089, 1995.

[27] D. S. Hall, D. J. Lockwood, S. Poirier, C. Bock, and B. R. MacDougall, "Raman and infrared spectroscopy of α and β phases of thin nickel hydroxide films electrochemically formed on nickel," *The Journal of Physical Chemistry A*, vol. 116, no. 25, pp. 6771–6784, 2012.

[28] J. W. Lee, J. M. Ko, and J.-D. Kim, "Hierarchical microspheres based on α-$Ni(OH)_2$ nanosheets intercalated with different anions: synthesis, anion exchange, and effect of intercalated anions on electrochemical capacitance," *The Journal of Physical Chemistry C*, vol. 115, no. 39, pp. 19445–19454, 2011.

[29] L. Xu, Y.-S. Ding, C.-H. Chen et al., "3D flowerlike α-nickel hydroxide with enhanced electrochemical activity synthesized by microwave-assisted hydrothermal method," *Chemistry of Materials*, vol. 20, no. 1, pp. 308–316, 2008.

[30] A. Delahaye-Vidal, B. Beaudoin, N. Sac-Epée, K. Tekaia-Elhsissen, A. Audemer, and M. Figlarz, "Structural and textural investigations of the nickel hydroxide electrode," *Solid State Ionics*, vol. 84, no. 3-4, pp. 239–248, 1996.

[31] C. V. Nunes Jr., M. Danczuk, A. A. Bortoti, J. M. Gonçalves, K. Araki, and F. J. Anaissi, "Unexpected effect of drying method on the microstructure and electrocatalytic properties of bentonite/alpha-nickel hydroxide nanocomposite," *Journal of Power Sources*, vol. 297, pp. 408–412, 2015.

[32] C. V. Nunes Jr., M. Danczuk, A. A. Bortoti et al., "Enhanced stability and conductivity of α-$Ni(OH)_2$/smectite clay composites," *Journal of the Electrochemical Society*, vol. 163, no. 10, pp. A2356–A2361, 2016.

[33] N. Iwashita and M. Inagaki, "Synthesis of nickel- and iron-hydroxide graphite intercalation compounds and their application to alkaline secondary battery," in *Chemical Physics of Intercalation*, A. P. Legrand and S. Flandrois, Eds., pp. 383–385, Springer, Boston, MA, USA, 1987.

[34] A. Babaei and A. R. Taheri, "Nafion/$Ni(OH)_2$ nanoparticles-carbon nanotube composite modified glassy carbon electrode as a sensor for simultaneous determination of dopamine and serotonin in the presence of ascorbic acid," *Sensors and Actuators B: Chemical*, vol. 176, pp. 543–551, 2013.

[35] J. M. Gonçalves, T. A. Matias, L. P. H. Saravia et al., "Synergic effects enhance the catalytic properties of alpha-$Ni(OH)_2$-FeOCPc@rGO composite for oxygen evolution reaction," *Electrochimica Acta*, vol. 267, pp. 161–169, 2018.

[36] W. Ma, R. Ma, C. Wang et al., "A superlattice of alternately stacked Ni–Fe hydroxide nanosheets and graphene for efficient splitting of water," *ACS Nano*, vol. 9, no. 2, pp. 1977–1984, 2015.

[37] D. S. Hall, D. J. Lockwood, C. Bock, and B. R. MacDougall, "Nickel hydroxides and related materials: a review of their structures, synthesis and properties," *Proceedings of the Royal Society A: Mathematical, Physical and Engineering Sciences*, vol. 471, no. 2174, article 20140792, 2014.

[38] M. S. Kim and K. B. Kim, "A study on the phase transformation of electrochemically precipitated nickel hydroxides using an electrochemical quartz crystal microbalance," *Journal of the Electrochemical Society*, vol. 145, no. 2, pp. 507–511, 1998.

[39] M. A. Rocha, F. J. Anaissi, H. E. Toma, K. Araki, and H. Winnischofer, "Preparation and characterization of colloidal $Ni(OH)_2$/bentonite composites," *Materials Research Bulletin*, vol. 44, no. 5, pp. 970–976, 2009.

[40] G. Wang, L. Zhang, and J. Zhang, "A review of electrode materials for electrochemical supercapacitors," *Chemical Society Reviews*, vol. 41, no. 2, pp. 797–828, 2012.

[41] J. Chang, H. Xu, J. Sun, and L. Gao, "High pseudocapacitance material prepared via in situ growth of $Ni(OH)_2$ nanoflakes on reduced graphene oxide," *Journal of Materials Chemistry*, vol. 22, no. 22, pp. 11146–11150, 2012.

[42] D.-L. Fang, Z. D. Chen, X. Liu, Z. F. Wu, and C. H. Zheng, "Homogeneous growth of nano-sized β-$Ni(OH)_2$ on reduced graphene oxide for high-performance supercapacitors," *Electrochimica Acta*, vol. 81, pp. 321–329, 2012.

[43] S. Min, C. Zhao, G. Chen, and X. Qian, "One-pot hydrothermal synthesis of reduced graphene oxide/$Ni(OH)_2$ films on nickel foam for high performance supercapacitors," *Electrochimica Acta*, vol. 115, pp. 155–164, 2014.

[44] Z. Sun and X. Lu, "A solid-state reaction route to anchoring $Ni(OH)_2$ nanoparticles on reduced graphene oxide sheets for supercapacitors," *Industrial & Engineering Chemistry Research*, vol. 51, no. 30, pp. 9973–9979, 2012.

[45] L. L. Zhang, Z. Xiong, and X. S. Zhao, "A composite electrode consisting of nickel hydroxide, carbon nanotubes, and reduced graphene oxide with an ultrahigh electrocapacitance," *Journal of Power Sources*, vol. 222, pp. 326–332, 2013.

[46] X. Zhu, Y. Zhong, H. Zhai, Z. Yan, and D. Li, "Nanoflake nickel hydroxide and reduced graphene oxide composite as anode materials for high capacity lithium ion batteries," *Electrochimica Acta*, vol. 132, pp. 364–369, 2014.

[47] M. A. Rocha, H. Winnischofer, K. Araki, F. J. Anaissi, and H. E. Toma, "A new insight on the preparation of stabilized alpha-nickel hydroxide nanoparticles," *Journal of Nanoscience and Nanotechnology*, vol. 11, no. 5, pp. 3985–3996, 2011.

[48] P. R. Martins, A. L. Araújo Parussulo, S. H. Toma, M. A. Rocha, H. E. Toma, and K. Araki, "Highly stabilized alpha-$NiCo(OH)_2$ nanomaterials for high performance device application," *Journal of Power Sources*, vol. 218, pp. 1–4, 2012.

[49] W. S. Hummers Jr. and R. E. Offeman, "Preparation of graphitic oxide," *Journal of the American Chemical Society*, vol. 80, no. 6, pp. 1339–1339, 1958.

[50] D. C. Marcano, D. V. Kosynkin, J. M. Berlin et al., "Improved synthesis of graphene oxide," *ACS Nano*, vol. 4, no. 8, pp. 4806–4814, 2010.

[51] F. J. Tölle, K. Gamp, and R. Mülhaupt, "Scale-up and purification of graphite oxide as intermediate for functionalized graphene," *Carbon*, vol. 75, pp. 432–442, 2014.

[52] A. Adán-Más, R. G. Duarte, T. M. Silva, L. Guerlou-Demourgues, and M. F. G. Montemor, "Enhancement of the Ni-Co hydroxide response as energy storage material by electrochemically reduced graphene oxide," *Electrochimica Acta*, vol. 240, pp. 323–340, 2017.

[53] Y. Si and E. T. Samulski, "Synthesis of water soluble graphene," *Nano Letters*, vol. 8, no. 6, pp. 1679–1682, 2008.

[54] J. Liang, H. Tan, C. Xiao, G. Zhou, S. Guo, and S. Ding, "Hydroxyl-riched halloysite clay nanotubes serving as substrate of NiO nanosheets for high-performance supercapacitor," *Journal of Power Sources*, vol. 285, pp. 210–216, 2015.

[55] B. Mendoza-Sánchez and Y. Gogotsi, "Synthesis of two-dimensional materials for capacitive energy storage," *Advanced Materials*, vol. 28, no. 29, pp. 6104–6135, 2016.

[56] S. Chen, J. Zhu, X. Wu, Q. Han, and X. Wang, "Graphene Oxide–MnO_2 nanocomposites for supercapacitors," *ACS Nano*, vol. 4, no. 5, pp. 2822–2830, 2010.

[57] J. Fang, M. Li, Q. Li et al., "Microwave-assisted synthesis of CoAl-layered double hydroxide/graphene oxide composite and its application in supercapacitors," *Electrochimica Acta*, vol. 85, pp. 248–255, 2012.